Nonlinear Dyn
https://doi.org/10.1007/s11071-024-10344-0

RESEARCH

Experimental validation of escape mechanisms in a bi-stable potential well

Attila Genda · Alexander Fidlin · Oleg Gendelman

Received: 9 August 2024 / Accepted: 12 September 2024

Abstract This paper experimentally studies escape mechanisms in a bi-stable potential well, focusing on critical forcing values depending on system damping, excitation frequency, and initial phase. The experimental setup has a rotational degree of freedom. It comprises a vertical shaft with adjustable air bearings and a copper disk that increases the moment of inertia and serves as an adjustable eddy current brake. The system also includes two coil springs that provide restoring moments. External momentum is provided by an electric motor controlled through a function generator. The paper describes the identification of system parameters and compares numerical and experimental results, validating previous theoretical and numerical findings regarding the *saddle* and *maximum escape mechanisms*.

Keywords Escape · Transient process · Experimental verification · Bi-stable potential well · Duffing oscillator

A. Genda (✉) · A. Fidlin
Institute of Engineering Mechanics, Karlsruhe Institute of Technology, Karlsruhe, Germany
e-mail: attila.genda@kit.edu

A. Fidlin
e-mail: alexander.fidlin@kit.edu

O. Gendelman
Mechanical Engineering, Technion - Israel Institute of Technology, Haifa, Israel
e-mail: ovgend@technion.ac.il

1 Introduction

Escape from a potential well is a fundamental problem in science and engineering, with applications ranging from celestial dynamics to the behavior of molecules. It is crucial in energy harvesting, transient resonance dynamics, and the stability of structures such as ships and MEMS devices [1–11].

The study of forced escape phenomena began with *Kramers*' work on thermal activation of chemical reactions in the 1940 s [12]. Significant challenges remain in understanding the escape process, even under quasi-steady-state conditions. Constant forcing can cause bifurcations due to slow variations in system parameters [6,13,14]. The situation is even more complicated if transients are involved due to small or no damping [15–17].

Analytical and numerical studies have extensively explored the escape dynamics of harmonically forced and damped particles [13,17–19]. Analytical expressions for escape criteria have been developed, although these often require empirical adjustments [20]. A notable observation in these studies is that the critical forcing amplitude curve usually exhibits a sharp minimum at frequencies lower than the natural frequency of small oscillations within the potential well, a pattern also seen in MEMS devices [6]. Two primary mechanisms for approaching the escape threshold have been identified: the *maximum mechanism*, where the trajectory reaches the boundary of the potential well, and the *saddle mechanism*, where the trajectory reaches a

Published online: 30 September 2024

saddle point on the resonance manifold, leading to a significant increase in response amplitude and subsequent escape [21–23].

Modern computational techniques have significantly advanced our understanding of dynamic systems. However, experimental validation remains crucial. Experiments provide concrete evidence supporting theoretical models and simulations, ensuring real-world accuracy.

There are only a few studies that experimentally investigate escape. Some of the most significant ones are presented below. *Shaw et al.* investigated 'roller-coaster' type models as analog devices for nonlinear oscillators [24], *Gottwald et al.* confirmed theoretical observations using a mechanical system to study escape from a potential well [25], and *Virgin et al.* illustrated nonlinear dynamics with a ball rolling on a surface [26].

More recent studies on vortex-induced vibrations have revealed escape phenomena similar to Duffing-type dynamics, enhancing our understanding of escape through both experiments and numerical computations [27–29].

In this paper, we extend the theoretical insights of [21–23,30] through experimental validation using a modified test rig of the Institute of Engineering Mechanics at the Karlsruhe Institute of Technology. This experiment aims to replicate theoretical conditions and provide a detailed analysis of escape mechanisms. We describe the experimental setup, followed by a detailed description of the parameter identification procedure for a double-well Duffing oscillator model.

We perform two types of experiments. The first one examines transient dynamics, starting with zero initial velocity in one of the stable equilibria and applying harmonic excitation with specific phase, amplitude, and frequency. A grid search in the amplitude-frequency plane explores escape conditions for two viscous damping values and two initial phases. The second series of experiments examines steady-state dynamics with a slowly increasing force amplitude, recording the smallest amplitude at which escape occurs. This procedure is done for two damping values, with the initial phase irrelevant.

Our setup offers precise damping control, which is essential for studying its impact on escape dynamics. In shaker-based systems, damping parameters are usually fixed and hard to adjust (cf. [24–26]). While an eddy current brake might provide control, the alteration in the equation of motion, experienced in shaker-based systems, complicates the comparison with the damped Duffing oscillator. Similarly, the modeling and controlling of friction is more straightforward in our current system.

The paper is structured as follows. Section 2 describes the fundamentals of a bistable potential well, the escape phenomenon and escape mechanisms. Section 3 describes the experimental setup. Section 4 details parameter identification and numerical model development. Section 5 compares experimental and numerical results. Section 6 discusses further examples of nonlinear phenomena observed in the measurements. Section 7 concludes the paper and gives scope for future research.

2 Theoretical background

The symmetric twin-well Duffing oscillator is a widely used mathematical model representing systems with two stable states of equal importance. It is often derived as the nonlinear Taylor series expansion of some more complex physical system [31]. The dynamics of a particle in the twin-well Duffing oscillator has several aspects. The conservative autonomous system is solvable in terms of Jacobi elliptic functions [32]. However, including damping forces and excitation complicates the problem such that only approximate analytical methods are viable. For example, [33] investigates the impacts of damping in the capture of a particle in one of the wells without external excitation using asymptotic methods.

On the other hand, [14] investigates the global dynamics of the excited, damped double-well Duffing oscillator in an extensive study showing for the first time that strange attractors can exist in second-order nonautonomous dynamical systems. Focusing on escape from one well introduces an asymmetry in the twin-well potential, although symmetric in complete form; thus, many findings about escape from an asymmetric potential well apply to this case as well [13]. Observations made by [34] for the weakening one-well potential, and later generalized by [35] for arbitrary polynomial potentials of order up to four, show that harmonically driven escape from conservative wells exhibit two primary escape mechanisms: the maximum mechanism and the saddle mechanism. *Farid and Gendelman* [17] revealed by multiple-scales analysis that these mechanisms also persist in the slightly damped case. In what follows, we give a simplified short theo-

retical overview of the level-crossing mechanisms for a symmetric, weakly nonlinear conservative potential based on [22]. By level crossing, we understand a weak definition of escape, in which some observable of the system (in our case, the displacement) leaves a safe zone. Please refer to the references above for a more comprehensive analysis and detailed derivations.

2.1 Example with quadratic-quartic potential

The equation of motion is given by

$$\ddot{x} + x - \varepsilon x^3 = f \sin(\Omega\tau + \beta), \tag{1}$$
$$x(0) = \dot{x}(0) = 0. \tag{2}$$

The absolute value of the critical displacement is one, that is,

$$\xi_{\text{crit},1,2} = \pm 1. \tag{3}$$

Assuming the excitation frequency is in the vicinity of the eigenfrequency of the linearized system and that the excitation force amplitude is small, i.e.

$$\Delta = \frac{\Omega - 1}{\varepsilon} \in O(1), \quad \text{and} \quad F = \frac{f}{\varepsilon} \in O(1), \tag{4}$$

we can apply the method of averaging. Assuming the motion is quasi-harmonic with slowly changing amplitude and phase difference, we can write

$$\begin{aligned} x &= A(t)\sin(\Omega\tau + \beta + \Psi(t)), \\ \dot{x} &= A(t)\cos(\Omega\tau + \beta + \Psi(t)). \end{aligned} \tag{5}$$

We apply the Van der Pol transformation to express the slow variables A and Ψ and note that the right-hand side only has small terms, thus, averaging the equations results in

$$\begin{aligned} \dot{\xi} &= -\frac{\varepsilon}{2} F \sin(\psi), \\ \psi &= -\varepsilon\Delta - \varepsilon\frac{3}{8}\xi^2 - \frac{\varepsilon}{2}\frac{F}{\xi}\cos(\psi), \end{aligned} \tag{6}$$

where $\xi = < A >$, $\psi = < \Psi >$ and $< \cdot >$ denotes the average. Elimination of the time yields the differential equation

$$\frac{\mathrm{d}\xi}{\mathrm{d}\psi} = \frac{F\sin(\psi)}{2\Delta + \frac{3}{4}\xi^2 + \frac{F}{\xi}\cos(\psi)}. \tag{7}$$

Eq. (7) is solved by

$$C(\psi, \xi) = \xi F \cos(\psi) + \Delta\xi^2 + \frac{3}{16}\xi^4 = \text{const.} \tag{8}$$

With zero initial conditions, we have $C(\psi, \xi) = 0$. Equation (8) is a first integral to the averaged equations, and its level sets determine the trajectories for any given initial condition on the $\psi - \xi$ phase cylinder. The level sets can be connected or disjoint depending on the parameters and initial conditions. The first case is simpler and leads to the maximum mechanism: for level crossing, the highest value of ξ along a trajectory must reach $\xi_{\text{crit}} = 1$. In the critical forcing case, based on Eq. (8), the trajectory becomes tangetial to $\xi = 1$, taking place either at $\psi = 0$ (for $\Delta \ll 0$, cf. Fig. 1a) or at $\psi = \pi$ (for $\Delta > 0$ or even for small negative Δ, cf. Fig. 1c). However, for slightly negative values of Δ, a saddle appears along $\psi = 0$ and the level set described by Eq. (8) can become disjoint (cf. Fig. 1b). Thus, an additional level-crossing condition becomes relevant. Reaching the critical level can only occur if $C_{\text{saddle}} > 0$, leading to the saddle mechanism. In summary, based on the above conditions, the critical forcing is given by

$$F_{\text{crit}}(\Delta) = \begin{cases} \Delta + \frac{3}{16} & \text{for } \Delta < \Delta_{\text{SM},2}, \\ \frac{8}{9}(-\Delta)^{3/2} & \text{for } \Delta_{\text{SM},2} \le \Delta \le \Delta_{\text{SM},1}, \\ -\Delta - \frac{3}{16} & \text{for } \Delta_{\text{SM},1} < \Delta, \end{cases} \tag{9}$$

with

$$\Delta_{\text{SM},1} = -\frac{9}{64}, \quad \text{and} \quad \Delta_{\text{SM},2} = -\frac{9}{16}. \tag{10}$$

Equation (9) is shown graphically in Fig. 2.

These two mechanisms seem universal for escape, as one might find them in various kinds of systems, not only in the example of the quadratic-quartic well [21,35,36].

3 Experimental setup

The following section describes the setup used to experimentally validate the two distinct escape mechanisms identified theoretically. The experiment utilizes a Duffing oscillator test rig (see Figs. 3, 4).

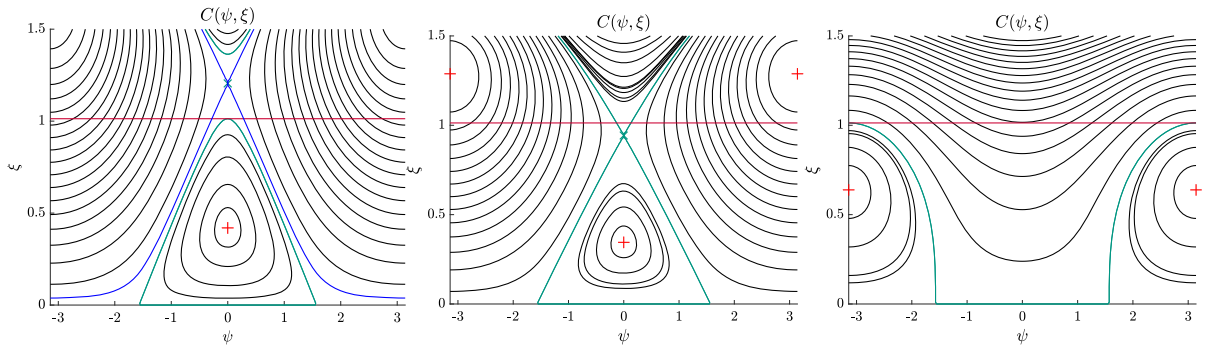

(a) Maximum mechanism for $\Delta = -0.8$ (b) Saddle mechanism for $\Delta = -0.5$ (c) Maximum mechanism for $\Delta = 0$

Fig. 1 Three types of mechanisms with critical forcing for different values of Δ and $\varepsilon = 0.05$. The level sets of $C(\psi, \xi)$ are represented in black, the trajectory with zero initial conditions in green, and the critical level in red. For (a), the saddle level set is shown in blue

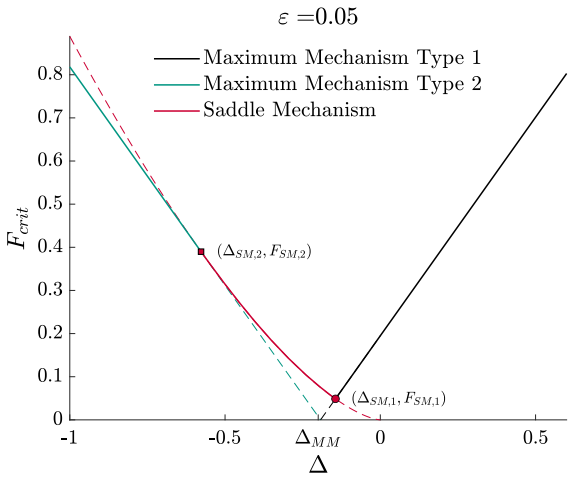

Fig. 2 Critical forcing amplitude depicted against the discrepancy between excitation frequency and the linearized natural frequency of the potential well for homogeneous initial conditions. Three concurring level-crossing mechanisms can be observed

Fig. 3 Experimental setup of a double-well oscillator created by the geometrical nonlinearities of coil springs

The configuration includes a vertical shaft equipped with two air bearings, which can be adjusted from 0 to 6 bars, to prevent radial displacement. In the absence of air pressure, the shaft is supported by ball bearings; as air pressure increases, the ball bearings disengage, considerably minimizing friction. The axial support of the shaft is provided by a ball bearing located at its bottom. A copper disk on the shaft serves a dual purpose; first, it increases the moment of inertia; second, when an electromagnet is activated, it generates viscous damping through eddy currents. A DC generator can adjust the damping strength by setting voltage U_D.

Two coil springs attach the shaft to the test rig frame, creating symmetric restoring moments and resulting in two stable equilibria in addition to an unstable one. The springs experience both compression and expansion. It is crucial to prevent excessive compression, as it can cause the springs to buckle, which would substantially change the system's behavior. A schematic is shown in Fig. 5. The system has a rotational degree of freedom φ. A disk with moment of inertia J is attached to a spring with stiffness c. In the unstable equilibrium, the com-

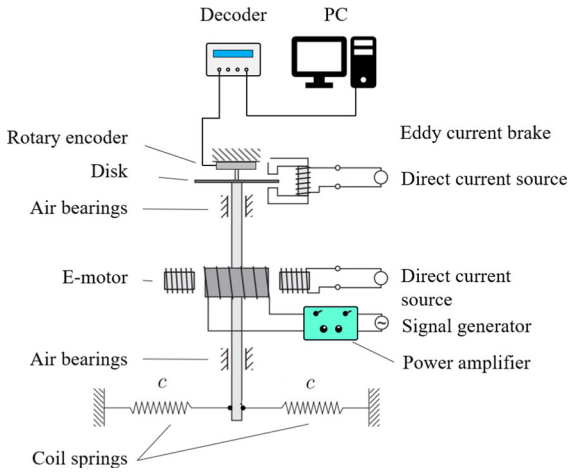

Fig. 4 Sketch of the experimental setup

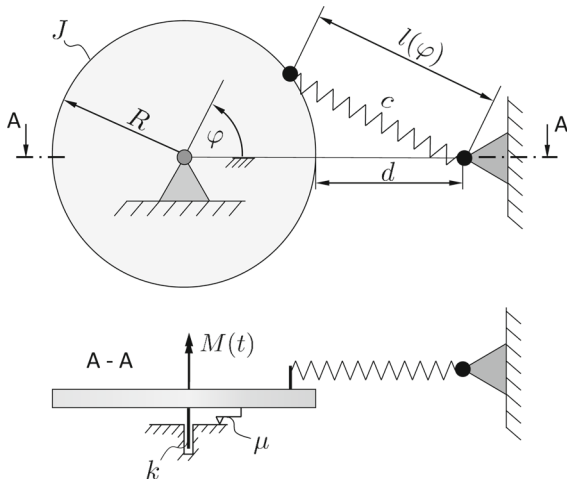

Fig. 5 Mechanical system schematic

pressed spring length is d; in the stable equilibrium, the relaxed spring length is l_0. The spring is fixed at a distance R from the center of the disk. The system experiences dry friction with coefficient μ and variable viscous damping with coefficient $k \in [k_{\min}, k_{\max}]$. With the eddy current brake off, $k = k_{\min}$.

An electric motor, consisting of an electromagnet as a stator and a copper core as a rotor, provides external momentum $M(t)$. The rotor voltage $u_M(t)$ is controlled by the signal of a function generator $u_S(t)$ augmented suitably by a power amplifier.

The motor torque is linearly proportional to the current of the rotor. The relationship between the voltage and the current of the motor can be described by the equation:

$$V = I R_m + L \frac{\mathrm{d}I}{\mathrm{d}t} + E, \tag{11}$$

where V is the applied voltage, I is the current, R_m is the motor's internal resistance, L is the inductance, and E is the back EMF. However, in our operating speed range, both inductive effects ($L\frac{\mathrm{d}I}{\mathrm{d}t}$) and back EMF ($E$) are negligible, which assumption simplifies the torque to a linear relationship with the applied voltage, as the dominant factor becomes the resistive voltage drop. Thus, precise motor torque control is achieved by directly varying the rotor voltage through the signal generator. However, within the specified frequency range, the power amplifier cannot be treated as a simple constant voltage multiplier. Therefore, a detailed power amplifier model will be provided in Sect. 4.1.

Measurement of the rotation angle and the signal generator's output voltage is essential for parameter identification. The rotation angle is measured with a 21-bit digital encoder from Netzer Precision using the SSI protocol. Data are read with an Arduino™ Mega 2560 Rev 3 and transferred via serial communication to MATLAB™. The Arduino board with an ADS1115 16-bit ADC measures the signal generator's output voltage. The setup supports a 200 Hz maximum sampling frequency, accurately capturing the mechanical system's dynamics. Measurements were taken at 100 Hz.

4 Parameter identification

Based on the mechanical model in Fig. 5, a mathematical model of the experiment must be formulated first to compare the experimental results with the numerical ones, resulting in the following equation of motion.

$$J\ddot{\varphi} + k\dot{\varphi} + \mu \mathrm{sign}\dot{\varphi} + cR(R+d)\times \left(1 - \frac{l_0}{\sqrt{2R^2 + d^2 + 2Rd - 2R(R+d)\cos\varphi}}\right) \times \sin\varphi = M(t). \tag{12}$$

The system's equilibria are in

$$\varphi_{1,2} = \{0, \pi\}, \tag{13}$$

$$\varphi_{3,4} = \pm \arccos\left(\frac{2R^2 + d^2 + 2Rd - l_0^2}{2R(R+d)}\right). \tag{14}$$

$\varphi_2 = \pi$ cannot exist with the physical values of the parameters since the spring does not allow such expansion. For $d < l_0$, the equilibrium $\varphi_1 = 0$ is unstable, and $\varphi_{3,4}$ are stable. We utilized a double-well Duffing model to simplify the model while maintaining accuracy. The simplified equation of motion is:

$$\begin{aligned}\ddot{\varphi}(t) + D\dot{\varphi}(t) + E\,\mathrm{sign}(\dot{\varphi})(t)) - A(\varphi(t) - C) \\ + B(\varphi(t) - C)^3 = F u_M(t).\end{aligned} \tag{15}$$

with parameters

- A – coefficient of the linear restoring moment,
- B – coefficient of the cubic restoring moment,
- C – bias term to align the coordinate system with the encoder's zero position,
- D – viscous damping coefficient per unit moment of inertia,
- E – dry friction coefficient per unit moment of inertia,
- F – voltage-torque proportionality factor per unit moment of inertia.

The excitation moment is not precisely known due to the missing motor torque constant, but modeling the system's dynamics can be done without it. By Ohm's law, the motor voltage $u_M(t)$ is linearly proportional to the current, neglecting back electromotive force and rotor inductance at low frequencies (cf. Fig. 6). Since the voltage is measured instead of the current, F is related but not equivalent to the torque constant.

Equation (15) describes a system with an unstable equilibrium at $\varphi_1 = C$ and stable equilibria at $\varphi_2 = C + \sqrt{A/B}$ and $\varphi_3 = C - \sqrt{A/B}$. The linearized angular eigenfrequency around each stable equilibrium is given by $\sqrt{2A}$. This equation holds for $\dot{\varphi} \neq 0$.

Parameters A, B, C, D, E, and F must be estimated to align the system with numerical simulations. Furthermore, since the direct measurement is not feasible, $u_M(t)$ needs to be assessed based on the recorded signal of the signal generator $u_S(t)$.

4.1 Estimation of the motor voltage

The Brüel & Kjær type 2706 power amplifier manual indicates that a constant voltage on the function generator does not produce motor torque and results in zero voltage on the rotor, as no current flows through the armature; the amplifier acts as a high-pass filter, reducing signals below 10 Hz [37]. Our experiment runs at 1.4 −2.5 Hz, where the amplifier still amplifies signals but with reduced and frequency-dependent amplification.

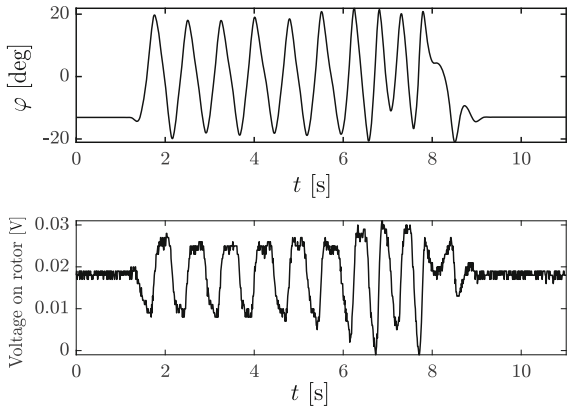

Fig. 6 Back electromotive force from manual shaft rotations, observed values are 2–3 orders of magnitude lower than experimental voltages

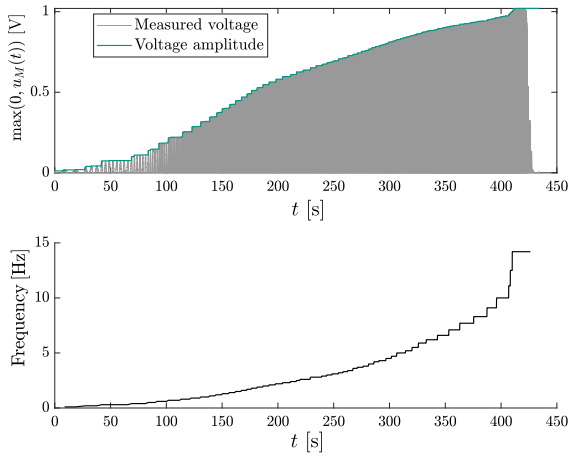

Fig. 7 Measurement of $u_M(t)$ at different frequencies of $u_S(t)$ with a constant 50 mV amplitude

Due to the absence of a Bode diagram in the power amplifier's datasheet, a measurement was performed to determine its amplification. A 50 mV harmonic voltage with varying frequency was generated and amplified. The output signal amplitude was measured for each frequency. Figure 7 shows the measurement data, and Fig. 8 depicts the amplification function.

For numerical analysis, the power amplifier was modeled using a DT_1 element with the transfer function

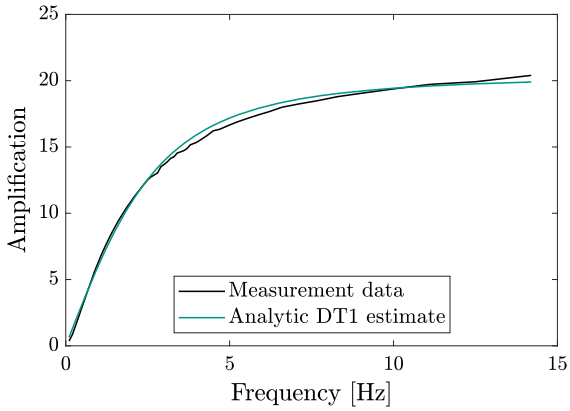

Fig. 8 Frequency-dependent amplification function of the power amplifier

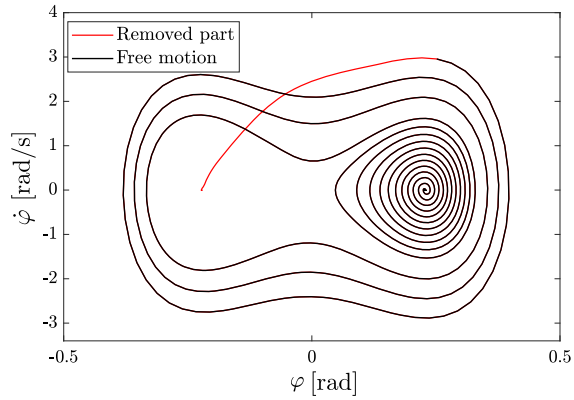

Fig. 9 Phase portrait of the shaft's rotation after manual perturbation

expressed as:

$$G(s) = \frac{K_D s}{1 + T_1 s}, \tag{16}$$

where $K_D = 1.02$ and $T_1 = 0.05$, based on measurements (cf. Fig. 8). The impulse response is defined as:

$$g(t) = \frac{K_D \delta(t)}{T_1} - \frac{K_D e^{-\frac{t}{T_1}}}{T_1^2}. \tag{17}$$

By substituting $s = \jmath\omega$, the amplification and phase shift can be calculated as:

$$G(\jmath\omega) = \frac{K_D \omega}{\sqrt{1 + T_1^2 \omega^2}} e^{\jmath \arctan \frac{1}{T_1 \omega}}, \tag{18}$$

leading to:

$$A(\omega) = \frac{K_D \omega}{\sqrt{1 + T_1^2 \omega^2}}, \qquad \theta(\omega) = \arctan \frac{1}{T_1 \omega}. \tag{19}$$

Assuming zero initial conditions, it becomes feasible to calculate the excitation signal $u_M(t)$ based on $u_S(t)$ and the transfer function.

$$U_M(s) = G(s) U_S(s) = \frac{K_D s}{1 + T_1 s} U_S(s),$$

$$u_M(t) = \mathcal{L}^{-1}\left\{ \frac{K_D s}{1 + T_1 s} U_S(s) \right\},$$

$$u_M(t) = \int_0^t g(t - \tau) u_S(\tau) d\tau,$$

$$u_M(t) = \frac{K_D}{T_1} \left(u_S(t) - \frac{1}{T_1} \int_0^t e^{-\frac{t-\tau}{T_1}} u_S(\tau) d\tau \right). \tag{20}$$

Equation (20) shows that $u_M(t)$ is not merely a scaled version of $u_S(t)$ but also includes an additional integral term. To identify the remaining parameters, the convolution integral will be numerically evaluated since the signal generator controls only the input of the power amplifier $u_S(t)$, not the motor voltage $u_M(t)$, thus $u_S(t)$ is considered the input and the results shall be interpreted accordingly.

4.2 Identification of the remaining parameters

The further parameter identification follows a two-step method. First, the parameters A, B, C, D, E and F are identified using measured acceleration. Then, estimates are refined by comparing measured to estimated angle values based on Eq. (15). Given precise angle measurement and low numerical differentiation noise, the parameters in Eq. (15) are determined using the least-squares method to minimize the squared errors between the measured and predicted acceleration values. For greater precision, initial parameter identification is performed without external excitation; first, the manually perturbed decaying motion is recorded; then the data are cleaned by removing the initial pushing phase to focus on free motion, as shown in Fig. 9.

This experiment is repeated multiple times, and the data is consolidated into a single vector with which the

following optimization problem is solved:

$$\min_{\mathbf{p}_a} J_a(\mathbf{t}; \mathbf{p}_a) = \frac{1}{N} \sum_{t_i \in \mathbf{t}} \left(\ddot{\varphi}(t_i) - \hat{\ddot{\varphi}}(t_i, \mathbf{p}_a) \right)^2, \qquad (21)$$

where N is the number of data points, $\mathbf{p}_a = [A, B, C, D, E]^\top$, and $\mathbf{t}$ contains all measurement time instances. The acceleration is estimated based on Eq. (15). Despite being a simplified version of Eq. (12) and only an approximation of the actual system, Eq. (15) has a high $R^2 = 0.996$, indicating that it closely approximates reality. The 2D surface for $U_D = 30\,V$ represented by $\hat{\ddot{\varphi}}(\varphi, \dot{\varphi})$ and the measured data is shown in Fig. 10.

Although this fit yields estimates for $[A, B, C, D, E]$, the values of D and E remain somewhat uncertain due to the similar effects of viscous and dry friction for energy dissipation at large-amplitude vibrations.

Instead, the dry friction coefficient E is estimated by simple static means: shifting the shaft out of its equilibrium at φ_3 to both directions and letting the spring to return it to equilibrium reveals the width of the stiction zone ($\Delta\varphi_3 = 0.4264° = 0.007442$ rad), where the dry friction exceeds the spring force which directly allows calculation of E. After the linearization of the conservative restoring force around φ_3 and assuming no external excitation, Eq. (15) can be written as:

$$\ddot{\varphi} + D\dot{\varphi} + E\,\mathrm{sign}(\dot{\varphi}) + 2A(\varphi - \varphi_3) = 0. \qquad (22)$$

At the angle corresponding to the half-width of the stiction region, the restoring torque equals the maximum friction value in equilibrium:

$$E_3 = \frac{2A\Delta\varphi_3}{2} = A\Delta\varphi_3 = 0.58. \qquad (23)$$

Repeating the static experiment around φ_2 results in a lower friction coefficient than this value; therefore, the final estimate for further numerical validation is $E = 0.5$.

Similarly, the parameter F can be identified. By exciting the system with a harmonic voltage, the resulting acceleration data, and its least-square fit is shown in Fig. 11.

A further step is to improve the parameter estimates obtained from acceleration data by minimizing the error between the measured angle data and the solution

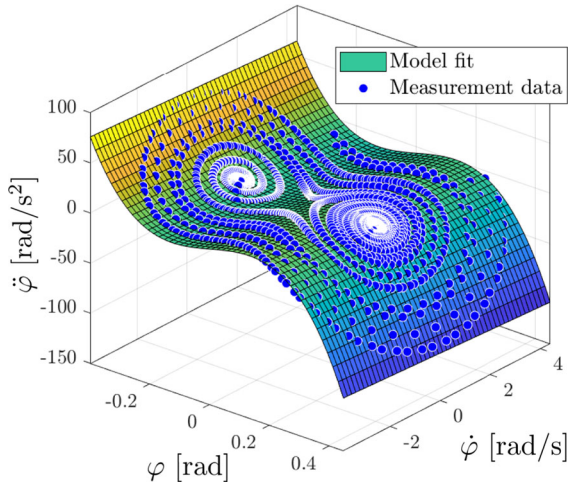

Fig. 10 Measured versus predicted angular acceleration values with added viscous damping ($U_D = 30\,V$)

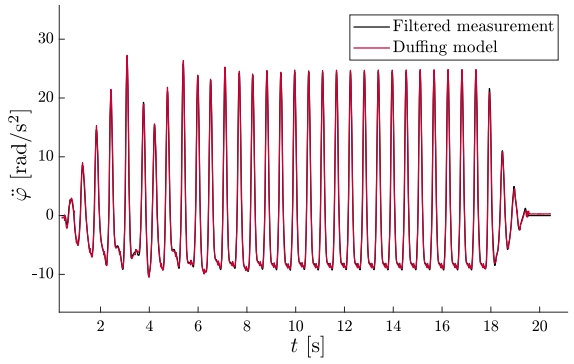

Fig. 11 Measured versus fitted data with an excitation frequency of $f = 1.75$ Hz, voltage range $\Delta u_S = 750$ mV, and starting phase $\beta = 0$, with additional damping ($U_D = 30\,V$). $R^2 = 0.999$

of Eq. (15) while including initial conditions in the optimization, estimated from the measured initial angle and the numerically calculated initial velocity. Figures 12, 13 show the results for both free and excited systems that match nearly perfectly. The estimated parameter values from distinct optimizations are close but never equal due to model sensitivities and noise. Therefore, in the numerical model, some rounded values that are close to the findings are used, as listed in Table 1.

Table 1 Optimal parameter values used in simulations

Parameters	$U_D = 0\,V$	$U_D = 30\,V$
A	84	84
B	1600	1600
C	0	0
D	0.25	1
E	0.5	0.5
F	-0.9	-0.9

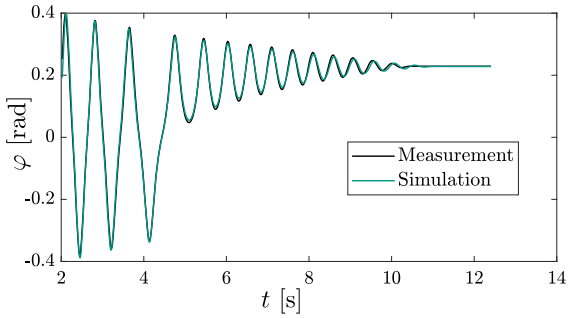

Fig. 12 Comparison of the measured data and numerical simulation with optimized parameters, without added damping

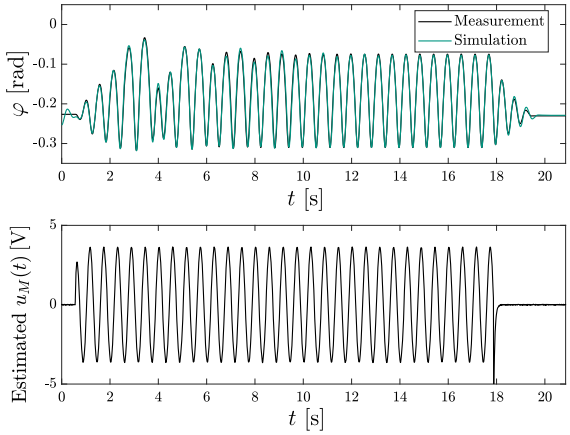

Fig. 13 Comparison of the measured data and numerical simulation with optimized parameters under external excitation $u_S(t) = 2.5 + 0.375\sin(1.75 \cdot 2\pi t)$ and added damping $U_D = 30\,V$. The initial motion before excitation is observed due to the Coulomb friction implementation in Eq. (15), valid only for $\dot{\varphi} \neq 0$

5 Model validation

5.1 Measurement of the critical $\Omega - F_S$ curve with initial conditions at a stable equilibrium

The following presents the measurement results for the critical forcing values. The shaft starts at φ_3. The signal generator is configured as follows:

$$u_S(t) = \begin{cases} \frac{F_S}{2}\sin(2\pi\Omega t + \beta), & \text{for } 0 \leq t \\ 0, & \text{for } t < 0, \end{cases} \tag{24}$$

with β as 0 or π. In practice, when starting an experiment, it has to be ensured that the signal generator voltage has been on zero for a sufficiently long time, letting any effect of the convoluted power amplifier signal decay. The numerical simulations assumed that the signal generator history was at zero voltage for $t \in (-\infty, 0]$. Two voltages were applied to the eddy current brake: $U_D = 0\,V$ or $U_D = 30\,V$. Escape was recorded if the shaft left the well corresponding to φ_3. Otherwise, if in 50 s the shaft did not leave, no escape was recorded since all transient processes had decayed. Figure 14 shows in deep blue color escape, in yellow no escape, and in turquoise the instances where both outcomes occurred under the same parameters in consecutive tests, indicating sensitivity near the escape boundary. Figure 15 presents the $\Omega - F_S$ curves from the numerical integration of the model with parameters from Table 1. Note that the power amplifier's frequency-dependent amplification factor is not included in the scale, but it was considered in the numerical simulations to approximate the system's dynamics.

The good agreement between experimental and simulation results, shown in Figs. 14, 15, respectively, validates the numerical system model. When comparing

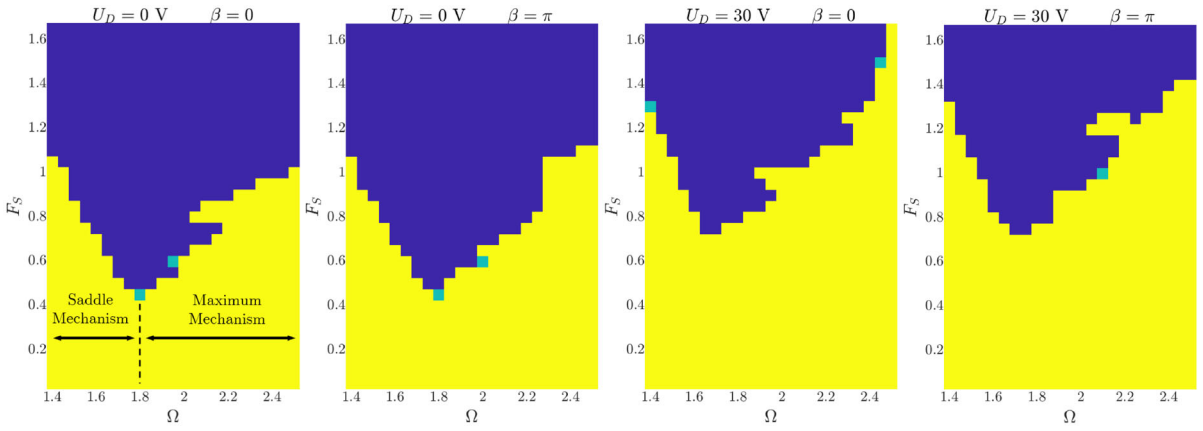

(a) $U_D = 0\,V$ and $\beta = 0$ (b) $U_D = 0\,V$ and $\beta = \pi$ (c) $U_D = 30\,V$ and $\beta = 0$ (d) $U_D = 30\,V$ and $\beta = \pi$

Fig. 14 Measured Ω [Hz] $- F_S$ [V] map with equilibrium initial conditions. $u_S(t) = \frac{F_S}{2}\sin(2\pi\,\Omega t + \beta)$. Yellow color shows no escape, blue shows escape, and turquoise shows both outcomes occurred with the same parameters in consecutive measurements

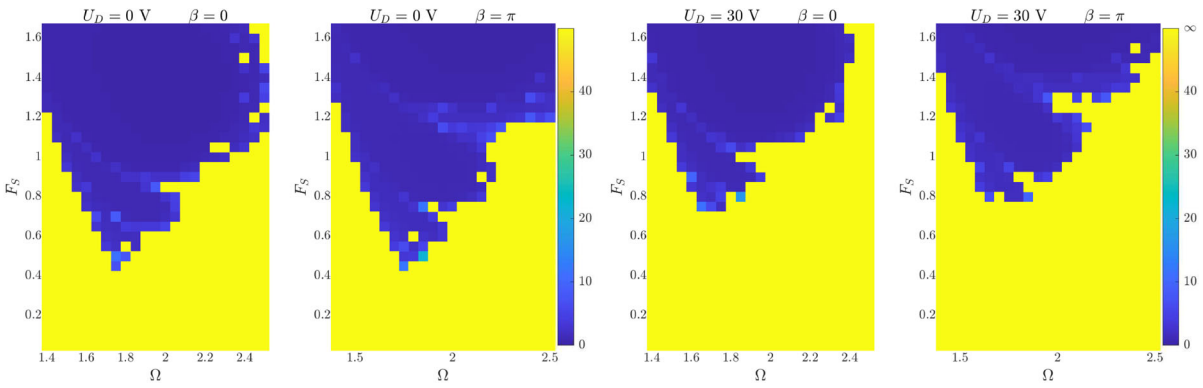

(a) $U_D = 0\,V$ and $\beta = 0$ (b) $U_D = 0\,V$ and $\beta = \pi$ (c) $U_D = 30\,V$ and $\beta = 0$ (d) $U_D = 30\,V$ and $\beta = \pi$

Fig. 15 Simulated Ω [Hz] $- F_S$ [V] map for $u_S(t) = \frac{F_S}{2}\sin(2\pi\,\Omega t + \beta)$ with equilibrium initial conditions ($\varphi(0) = \varphi_3$ and $\dot{\varphi}(0) = 0$). The color scale shows the escape time. Yellow indicates that there was no escape within 50 s

the figures, the following similarities in the critical excitation amplitudes between the numerical and experimental results are observed:

- On the right branch of the V-shaped curve, the maximum mechanism prevails, meaning that the amplitude directly grows until it reaches the potential boundary (cf. Fig. 15a). On the left branch of the V-shaped curve, the saddle mechanism dominates, meaning that, in the beginning, the amplitude seems to converge to some stationary value, still far from the potential boundary. However, it suddenly increases without caution and reaches the potential boundary (cf. Fig. 17).
- A marked minimum occurs, with the critical forcing boundary on the $\Omega - F_S$ plane forming a V-shape that is uneven on its right-hand side due to the maximum mechanism, caused by separatrix crossing resulting in a cascade of period-doubling bifurcations and subsequent chaos [13]
- The curve's minimum shifts left from the linearized eigenfrequency. At φ_3, this is $\sqrt{2A} = 12.96$ rad/s $= 2.06$ Hz, while the measured minimum is $1.7 - 1.8$ Hz, depending on damping.
- To the right of the critical force's minimum, the boundary distinguishing the escape and non-escape zones is irregular. Parameter regions with escape (blue 'bays') and no escape (yellow 'peninsulas')

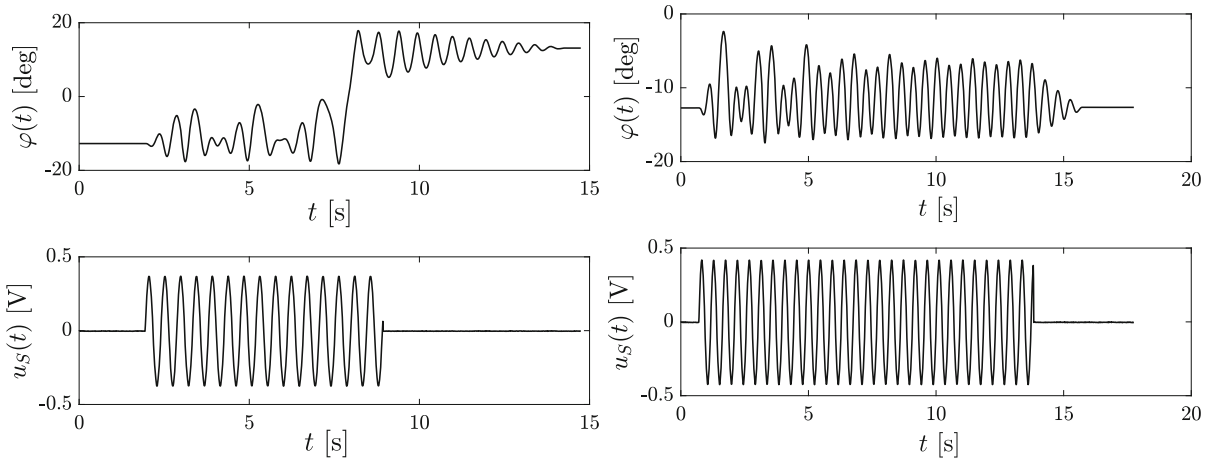

(a) Escape 'bay' with $F_S = 375$ mV (b) No-escape 'peninsula' with $F_S = 425$ mV

Fig. 16 Time series comparison of measurements with parameters from an escape 'bay' and a no-escape 'peninsula' for $\Omega = 2.15$ Hz, $U_D = 0$ V, $\beta = 0$. The top graph illustrates the rotation angle, while the bottom graph shows the excitation signals

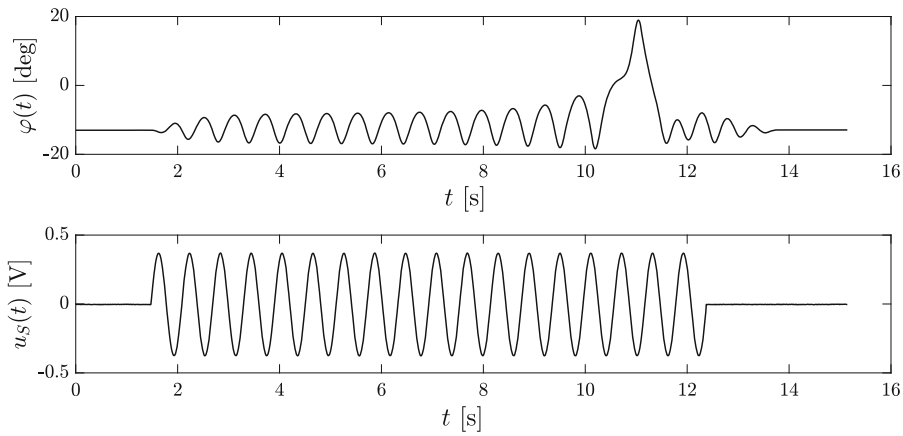

Fig. 17 Experimental time-series data showing escape through the saddle mechanism for $F_S = 375$ mV, $\Omega = 1.65$ Hz, $U_D = 30$ V, $\beta = 0$.The top graph illustrates the rotation angle, while the bottom graph shows the excitation signals

mix together. In this way, an increase in the excitation amplitude can cause an escaping scenario to 'stabilize' and revert to a non-escaping one (passing from a 'bay' to a 'peninsula' when moving upward in the diagram).

– The initial phase β minimally impacts the location of the V-shaped critical forcing curve, mainly affecting the curve's right-hand side.
– The required excitation amplitude increases with damping, from $F_S = 0.4$ without damping to $F_S = 0.7$ with damping. The damping also shifts the curve's minimum left from 1.8 Hz to 1.7 Hz.
– Escape 'bays' and no-escape 'peninsulas' persist with increased viscous damping (cf. Fig. 16). A larger excitation amplitude can increase the vibration amplitude more rapidly. Still, the highest envelope point is not necessarily always greater than the one corresponding to a smaller excitation amplitude, as the latter's peak may occur sooner, allowing transients to decay further. Changing the initial excitation phase shows that the V-shape's location and form are consistent near the sharp minimum. Still, the curve changes farther away, especially on the right-hand side of the curve, aligning with numerical predictions (cf. Figs. 14, 15).

These experimental results match the findings of many previous numerical and analytical studies on the location and shape of the critical forcing curve [17,21,22].

5.2 Determination of the critical $\Omega - F_S$ curve for quasi-steady excitation amplitude

This section determines the critical excitation amplitude for escape without transient effects by gradually increasing the harmonic excitation amplitude and allowing the transients to subside. Depending on the excitation frequency, the so-far-attracting periodic solution loses stability at a certain amplitude, leading to rapid escape (saddle mechanism) or a period-doubling cascade and chaos (maximum mechanism). This latter phenomenon is related to the crossing of the separatrix and was accurately described analytically by Melnikov analysis for a similar damped bi-stable Duffing oscillator [14].

To provide conditions similar to the experimental ones, in simulations, the function generator's output is

$$u_S(t) = \frac{F_{\max}}{2} \frac{t}{t_{\max}} \sin(2\pi \Omega t), \tag{25}$$

where $F_{\max}$ and $t_{\max}$ are sufficiently large to ensure that the particle is driven out of its initial well with a quasi-statically increasing amplitude.

Figure 18 shows the critical forcing amplitude values for the numerical and experimental results, indicating a sharp minimum that simulations accurately predict. This minimum is shifted when the eddy current brake acts with additional viscous damping on the system (cf. Fig. 18b). The excitation amplitude increases from $F_S = 0.5$ V to $F_S = 0.8$ V, and the frequency shifts leftward from approximately $\Omega_{\min} = 1.75$ Hz to $\Omega_{\min} = 1.65$ Hz, which is significant considering the system's linearized eigenfrequency of about $\Omega_{\text{lin}} = 2.05$ Hz.

The initial excitation phase is irrelevant because the system's vibrations quickly adapt, as evidenced in experiments and simulations, with or without viscous damping, as shown in Figs. 19, 20.

6 Further observations and discussion

In addition to the experimentally observed escape mechanisms reported in the previous section, several other nonlinear phenomena were observed in this simple system. We report on the most interesting ones in the following.

Figure 21 shows the amplitude increasing slowly, then rapidly, nearly reaching the saddle but falling back. Over several cycles, the transients damp out, leading to periodic motion. In contrast, Fig. 22 shows a rather chaotic scenario in which the system escapes from its initial well after more than 30 excitation periods. In Fig. 23, another example is given to illustrate the sensitivity and chaotic behavior of the system, showing that it can either stay in the original well or escape despite seemingly unchanged ambient conditions.

Although escape time was not directly measured, a trajectory's escape is usually determined within the first few excitation periods. Numerical simulations confirm that escape times longer than 20 s are rare, with few trajectories persisting within the well for more than 30-50 excitation periods. Such trajectories, if any, are chaotic, as shown in Fig. 22. Typically, if a trajectory does not escape within the first few attempts, as shown in Figs. 15b and 21, it reaches a periodic steady state vibration due to damping. However, unlike the linear system investigated in [15], escape can still occur later due to large nonlinearities, as shown in Figs. 15a, where only the third amplitude envelope peak resulted in escape.

Measurement data suggest several attractors in the phase space, with complex interconnected regimes that depend on initial conditions, system parameters, and excitation parameters. As shown in Fig. 24, there is a coexistence of periodic solutions and possibly chaotic attractors, a determination that is challenging to make based on experiments due to the long transients before reaching a periodic solution. For example, Fig. 25 presents data where the motion does not exhibit discernible patterns, making it uncertain whether continued observation would reveal a periodic solution.

It should be noted that the above findings highlight deviations from the 1:1 resonance regime, indicating that the actual escape dynamics is more complex than the one dictated by pure 1:1 transient resonance.

7 Conclusions and scope for future research

This research aimed to experimentally confirm the escape mechanisms documented in the literature [13, 21,22] by developing a setup comprising a test rig with a high precision capacitive angle encoder, precisely adjusted viscous damping through eddy currents, and an electromotor applying arbitrary-shaped torque,

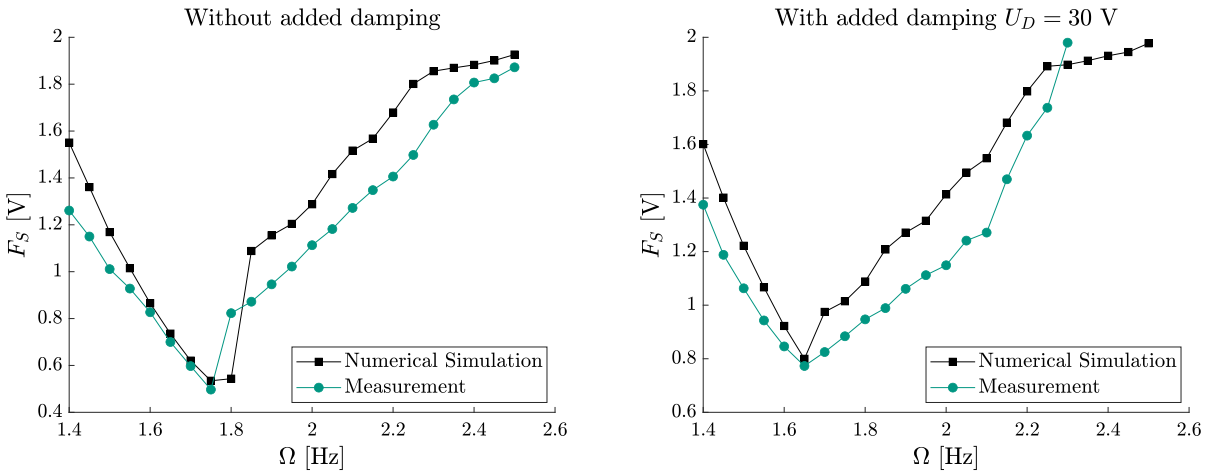

(a) Without additional damping

(b) With additional damping $U_D = 30$ V

Fig. 18 Comparison of numerical results with experimental ones by gradually increasing the excitation amplitude and noting its value at the point of escape. Despite some quantitative differences, the prediction of the sharp minimum's location and value shows good agreement

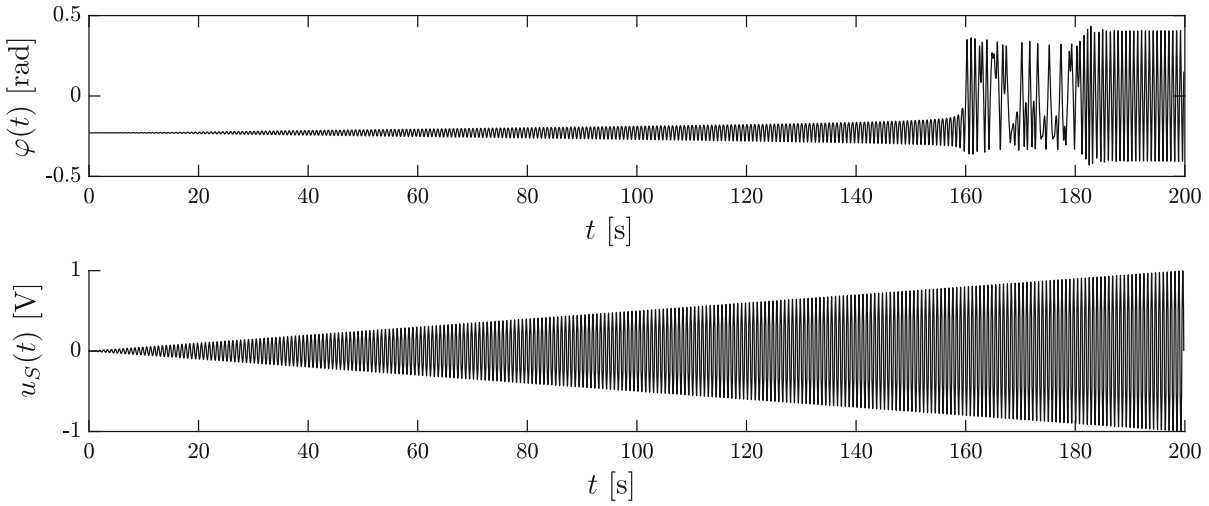

Fig. 19 Numerical simulation time-series data with amplitude sweep at $\Omega = 1.4$ Hz, $D = 1$. The initial phase is irrelevant in this case. Escape occurs at $F_{\mathrm{S,crit}} = 1.601$ V. The saddle mechanism is observed, with a sudden increase in oscillation amplitude occurring far from the well's boundary. After the transient process following the escape, the solution stabilizes around a periodic, full-well oscillation

using a double-well Duffing oscillator model for system identification and validation. The chosen experimental setup is simpler than many previous experiments [24–26], yet more universal, as damping (with simple modifications, even friction) can be precisely controlled. Furthermore, the excitation can take an arbitrary shape and is not limited to a harmonic one.

The experimental findings reveal several key aspects. First, the two analytically found escape mechanisms, the saddle and maximum mechanisms, were confirmed by experiments. The saddle mechanism allows escape without precaution in both types of experimental setups. Meanwhile, the maximum mechanism is identifiable through large oscillations approaching the

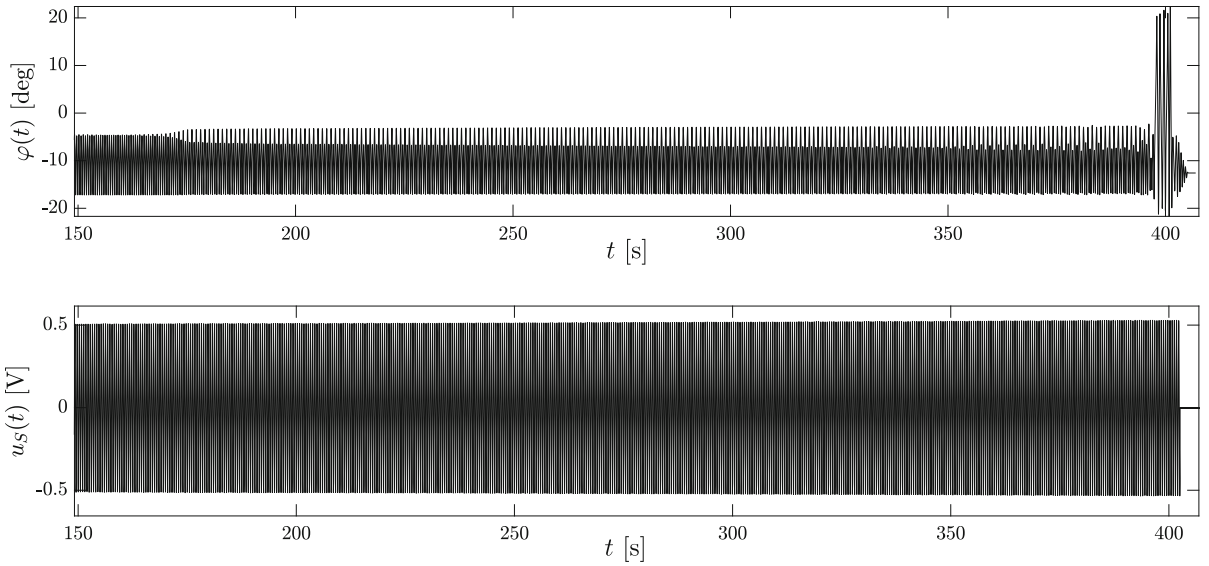

Fig. 20 Experimental time-series data with amplitude sweep at $\Omega = 2.0$ Hz, $U_D = 0$ V. Escape occurs at $F_{\mathrm{S,crit}} = 1.070$ V. Before escape, a cascade of period-doubling bifurcations is observed

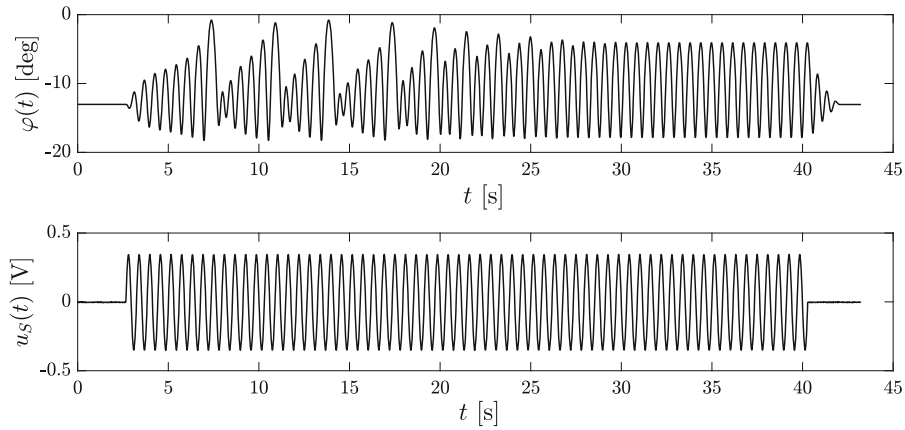

Fig. 21 Non-escaping experimental scenario where both the saddle and the maximum mechanism are insufficient to lead to an escape with $F_S = 350$ mV, $\Omega = 1.7$ Hz, $U_D = 30$ V, $\beta = 0$

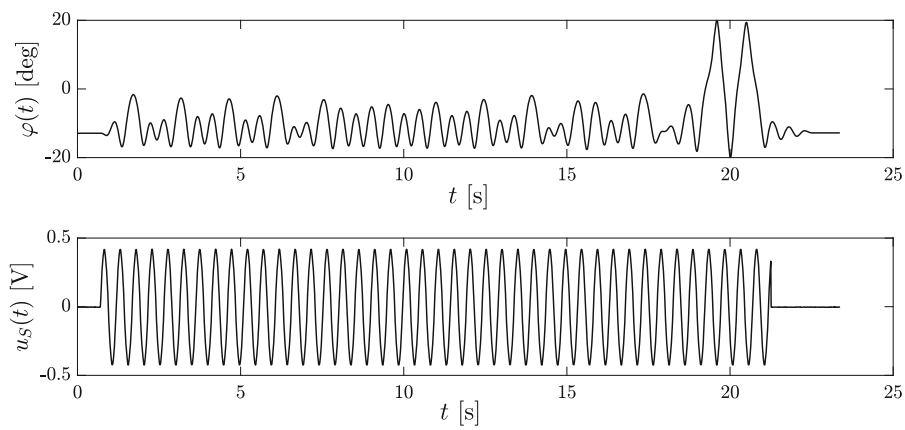

Fig. 22 Experimental time-series data of chaotic escape through the maximum mechanism for $F_S = 425$ mV, $\Omega = 2.05$ Hz, $U_D = 0$ V, $\beta = 0$

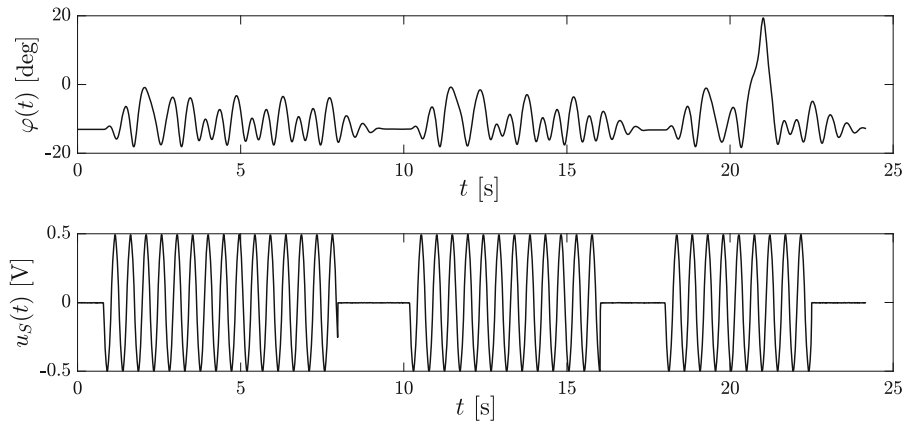

Fig. 23 A chaotic experimental scenario where, under the same parameters and initial conditions, the system sometimes remains within the well and sometimes escapes. $F_S = 500$ mV, $\Omega = 2.1$ Hz, $U_D = 30$ V, $\beta = \pi$

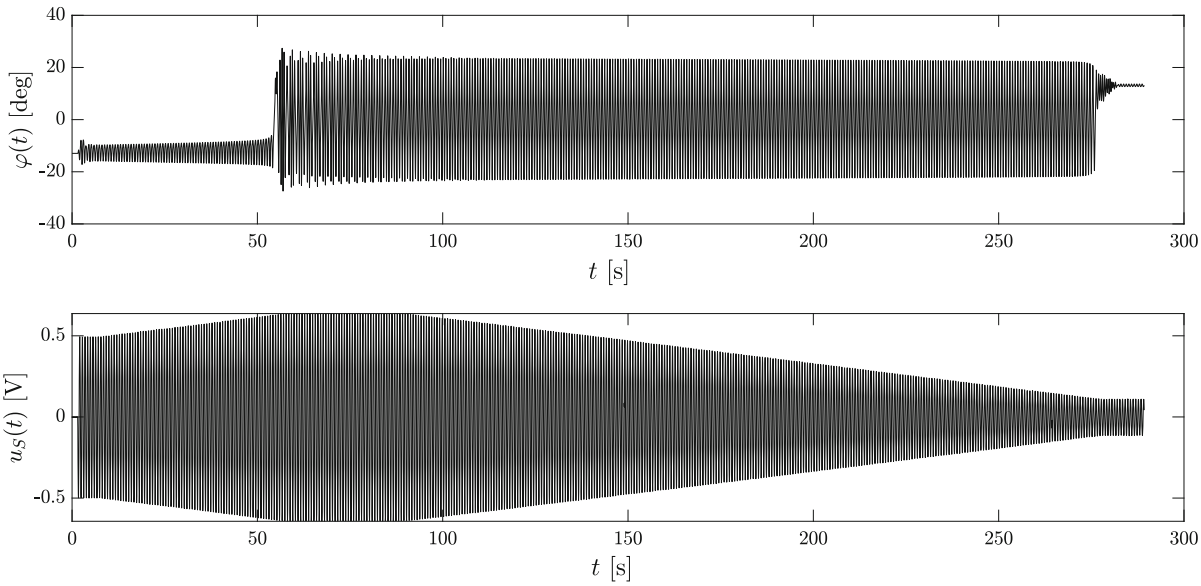

Fig. 24 Time-series data with amplitude sweep at $\Omega = 1.4$ Hz, $U_D = 0$ V. Initial phase is irrelevant. Escape occurs at $F_{\mathrm{S,crit}} = 1.244$ V. The saddle mechanism shows a sudden increase in oscillation amplitude far from the well boundary. After transient decay, periodic full-well oscillation stabilizes and remains stable even when excitation amplitude is reduced. Upon losing stability, vibrations continue in a single well with reduced amplitude

potential well boundary. When the excitation amplitude gradually increases, an additional cascade of period-doubling bifurcations may also be observed. These effects remain robust even with increasing damping; however, the minimum of the V-curve shifts to higher forces and lower frequencies.

Second, a good alignment between the experimental results and the simulations could only be reached through thorough analysis and modeling of the entire experimental setup, including the power amplifier, the electric motor, and the mechanical system. A careful analysis of friction mechanisms would be necessary to improve the theoretical model further.

Third, irregular escape boundaries, such as nonescaping 'peninsulas' and escape 'bays,' are accurately identified. The occurrence of 'peninsulas' and 'bays' is likely associated with the phase of the oscillations. It is important to recall that these experiments are designed with a suddenly activated forcing signal, the phase of which can have an effect on the escape behavior. Furthermore, when started in equilibrium, the appearance of escape 'bays' at lower amplitude values (cf. Fig. 14)

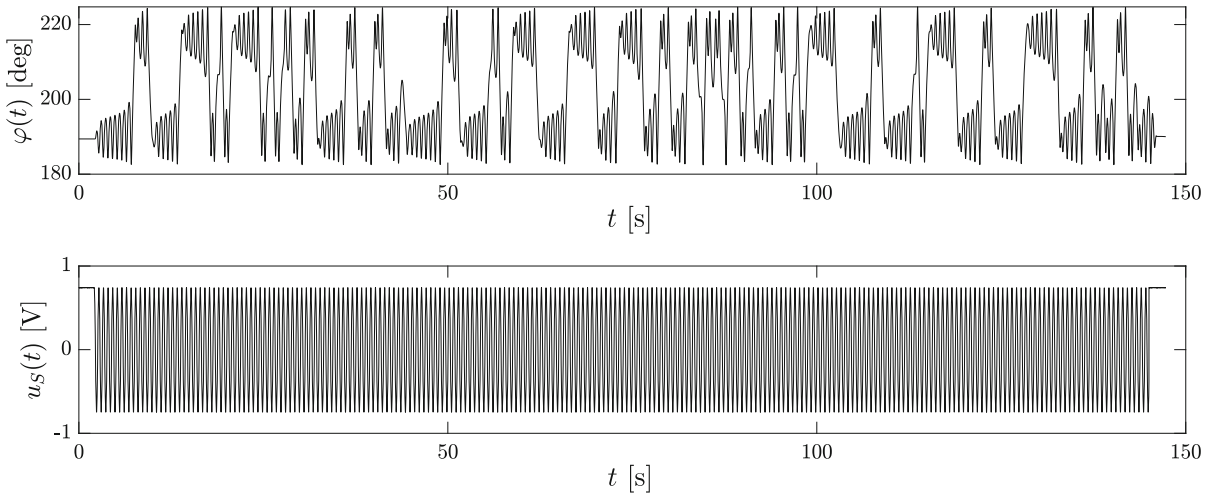

Fig. 25 Measured time-series data with harmonic excitation. $\Omega = 1.6$ Hz, $F_S = 1.5$ V, $U_D = 30$ V, $\beta = \pi/2$ and added dry friction (non-quantified). The motion appears chaotic and does not settle into a recognizable pattern

than those needed for escape from a quasi-steady-state solution (cf. Fig. 18) suggests that transients induce escape in this regime, as the vibration envelope exhibits several peaks before reaching a periodic steady-state solution.

This research opens several promising avenues for future studies. The proximity of 1:1 resonance was examined, but the potential for sub- or super-harmonic resonance and its impact on the critical $\Omega - F$ curve is also a fascinating topic. Investigating escape under frequency-modulated signals, particularly sweep signals, is of significant technical importance since machinery operating at a specific speed must pass through resonance to reach its operational point. Similarly, power-off involves passing through resonance in the opposite direction. Understanding the dynamics of the saddle and maximum mechanisms can help anticipate system responses in both directions.

Acknowledgements We acknowledge the assistance of AI tools, including OpenAI's ChatGPT (version GPT-4o), Grammarly, and Writefull, for language editing and refinement in preparing this article.

Author contributions A.G. and A.F. conceptualized the experiment. A.G. built up and conducted the experiment and analyzed the data. A.G. wrote the main manuscript text and prepared all figures. All authors reviewed the manuscript.

Funding Open Access funding enabled and organized by Projekt DEAL. This research was funded by the Deutsche Forschungsgemeinschaft (DFG, German Research Foundation) under Project Number 508244284. We are sincerely grateful for their support.

Data availability Data supporting the findings of this study are available from the corresponding author upon reasonable request and subject to the author's discretion.

Declarations

Conflict of interest The authors declare that they have no conflict of interest.

References

1. Mann, B.: Energy criterion for potential well escapes in a bistable magnetic pendulum. J. Sound Vib. **323**, 864 (2009)
2. Quinn, D.: Transition to escape in a system of coupled oscillators. Int. J. Non-Linear Mech. **32**, 1193 (1997)
3. Rega, G., Lenci, S.: Dynamical integrity and control of nonlinear mechanical oscillators. J. Vib. Control **14**, 159 (2008)

4. Barone, A., Patemo, G.: Physics and applications of the Josephson effect. Wiley, New York (1982)
5. Belenky, V., Sevastianov, N.: Stability and safety of ships-risk of capsizing. The Society of Naval Architects and Marine Engineers, Jersey City (2007)
6. Elata, D., Bamberger, H.: On the dynamic pull-in of electrostatic actuators with multiple degrees of freedom and multiple voltage sources. J. Microelectromech. Syst. **15**, 1310 (2006)
7. Bethe, H., Brown, G., Applegate, J., Lattimer, J.: Equation of state in the gravitational collapse of stars. Nucl. Phys. A **324**(2), 487 (1979). https://doi.org/10.1016/0375-9474(79)90596-7
8. Castagnino, M., Ferraro, R.: The radiation from moving mirrors: the creation and absorption of particles. Ann. Phys. **154**, 1 (1984). https://doi.org/10.1016/0003-4916(84)90139-8
9. Thompson, J., Hunt, G., Tvergaard, V.: Elastic instability phenomena. J. Appl. Mech. **52**, 241 (1985). https://doi.org/10.1115/1.3169017
10. Virgin, L.: The nonlinear rolling response of a vessel including chaotic motions leading to capsize in regular seas. Appl. Ocean Res. **9**(2), 89 (1987). https://doi.org/10.1016/0141-1187(87)90011-3
11. Orlando, D., Gonçalves, P., Lenci, S., Rega, G.: Influence of the mechanics of escape on the instability of von Mises truss and its control. Proc. Eng. **199**, 778 (2017). https://doi.org/10.1016/j.proeng.2017.09.048
12. Kramers, H.A.: Brownian motion in a field of force and the diffusion model of chemical reactions. Physica **7**(4), 284–304 (1940)
13. Thompson, J.M.T.: Chaotic phenomena triggering the escape from a potential well. Proc. Royal Soc. London A **421**, 195 (1989)
14. Holmes, P.: A nonlinear oscillator with a strange attractor. Philosophical Trans. Royal Soc. London Ser. A Math. Phys. Sci. **292**(1394), 419–448 (1979)
15. Genda, A., Fidlin, A., Gendelman, O.: The level-crossing problem of a weakly damped particle in quadratic potential well under harmonic excitation. Nonlinear Dyn. **111**, 20563 (2023). https://doi.org/10.1007/s11071-023-08875-z
16. Genda, A., Fidlin, A., Gendelman, O.: Dynamics of forced escape from asymmetric truncated parabolic well. ZAMM - J. Appl. Math. Mech. / Zeitschrift für Angewandte Mathematik und Mechanik (2023). https://doi.org/10.1002/zamm.202200567
17. Farid, M., Gendelman, O.: Escape of a forced-damped particle from weakly nonlinear truncated potential well. Nonlinear Dyn. **103**, 63 (2021). https://doi.org/10.1007/s11071-020-05987-8
18. Thompson, J.: In *Engineering applications of dynamics of Chaos*, *CISM Courses and Lectures*, vol. 139, ed. by W. Szemplinska-Stupnicka, H. Troger Springer, Berlin, (1991), pp. 279–309
19. Sanjuan, M.: The effect of nonlinear damping on the universal escape oscillator. Int. J. Bifurc. Chaos **9**, 735 (1999)
20. Virgin, L., Plaut, R., Cheng, C.: Prediction of escape from a potential well under harmonic excitation. Int. J. NonLinear Mech **27**, 357 (1992). https://doi.org/10.1016/0020-7462(92)90005-R
21. Gendelman, O.: Escape of a harmonically forced particle from an infinite-range potential well: a transient resonance. Nonlinear Dyn. **93**, 79 (2018). https://doi.org/10.1007/s11071-017-3801-x
22. Gendelman, O., Karmi, G.: Basic mechanisms of escape of a harmonically forced classical particle from a potential well. Nonlinear Dyn. **98**, 2775 (2019). https://doi.org/10.1007/s11071-019-04895-9
23. Karmi, G., Kravetc, P., Gendelman, O.: Analytic exploration of safe basins in a benchmark problem of forced escape. Nonlinear Dyn. **106**, 1573 (2021). https://doi.org/10.1007/s11071-021-06942-x
24. Shaw, S., Haddow, A.: The dynamics of 'roller-coaster' type experimental models used as analog devices for nonlinear oscillators. Nonlinear Dyn. **3**, 123 (1991)
25. Gottwald, J., Virgin, L., Dowell, E.: Experimental mimicry of Duffing's equation. J. Sound Vib. **158**, 447 (1992). https://doi.org/10.1016/0022-460X(92)90419-X
26. Virgin, L., Lyman, T., Davis, R.: Nonlinear dynamics of a ball rolling on a surface. Am. J. Phys. **78**, 321 (2009)
27. Alhussein, H., Daqaq, M.F.: Potential well escape via vortex-induced vibrations: a single-degree-of-freedom analysis. Phys. D: Nonlinear Phenom. **426**, 133001 (2021). https://doi.org/10.1016/j.physd.2021.133001
28. Alhussein, H., Daqaq, M.F.: Escape of a circular cylinder from a potential well via nonlinear vortex-induced vibrations: an experimental investigation. J. Sound Vib. **539**, 117239 (2022). https://doi.org/10.1016/j.jsv.2022.117239
29. Alhussein, H., Laws, P., Daqaq, M.F.: On the escape from a potential well via vortex-induced vibrations: a computational approach. J. Fluids Struct. **108**, 103424 (2022). https://doi.org/10.1016/j.jfluidstructs.2021.103424
30. Karmi, G., Kravetc, P., Gendelman, O.: Analytic exploration of safe basins in a benchmark problem of forced escape. Nonlinear Dyn. **106**, 1573–1589 (2021)
31. Moon, F., Holmes, P.: A magnetoelastic strange attractor. J. Sound Vib. **65**(2), 275 (1979). https://doi.org/10.1016/0022-460X(79)90520-0
32. Kovacic, I.: *Nonlinear oscillations: exact solutions and their approximations*, 1st edn. Engineering (Springer Cham, Switzerland, 2020). https://doi.org/10.1007/978-3-030-53172-0
33. Bourland, F.J., Haberman, R.: Separatrix crossing: time-invariant potentials with dissipation. SIAM J. Appl. Math. **50**(6), 1716–1744 (1990)
34. Genda, A., Fidlin, A., Gendelman, O.: On the escape of a resonantly excited couple of particles from a potential well. Nonlinear Dyn. **104**, 91 (2021). https://doi.org/10.1007/s11071-021-06312-7
35. Kravetc, P., Gendelman, O.: Approximation of potential function in the problem of forced escape. J. Sound Vib. **526**, 116765 (2022). https://doi.org/10.1016/j.jsv.2022.116765
36. Farid, M.: Escape dynamics of a particle from a purely nonlinear truncated quartic potential well under harmonic excitation. Nonlinear Dyn. **111**(4), 3035–3051 (2023)
37. Bruel & Kjaer. *Bruel & Kjaer 2706 Data Sheet*. https://www.atecorp.com/ATECorp/media/pdfs/data-sheets/Bruel-Kajaer-2706_Datasheet.pdf (2024). Accessed: 2024-07-15